OXYGEN ISOTOPIC IMAGING OF REFRACTORY INCLUSIONS FROM THE MILLER RANGE (MIL) 090019 CO3 CHONDRITE: A PEROVSKITE PERSPECTIVE. P. Mane[1,2] , A. N. Nguyen[2,3], D. K. Ross[2,3] and J. I. Simon[2], [1]Lunar and Planetary Institute, USRA, 3600 Bay Area Boulevard, Houston, TX 77058 USA (pmane@lpi.usra.edu), [2]EISD/Astromaterials Research and Exploration Sciences, NASA Johnson Space Center, 2101, NASA Parkway, Houston, TX 77058 USA, [3]Jacobs, NASA Johnson Space Center, Houston, TX, 77058, USA. [4]Univ. Texas El Paso – Jacobs JETS contract, NASA JSC, Houston TX 77058.

Introduction: Calcium-Aluminum-rich Inclusions (CAIs) in primitive meteorites are the first solids to condense in the Solar System [e.g., 1,2]. The oxygen isotopic compositions recorded in various mineral components of CAIs provide clues about their origins and post-formation histories, recording processes such as condensation, melting, nebular alteration, and fluid-rock reactions on the parent body [e.g., 3].

MIL 090019 is similar to some rare carbonaceous chondrites such as Acfer 094 [4, 5], DOM 08004/6 [6] and ALH 77303 [7] that contain high abundances of a variety of refractory inclusions. This provides an opportunity to study the oxygen isotopic record of different types of refractory inclusions within the same meteorite. We analyzed CAIs specifically targeting primary minerals that are direct nebular condensates, such as corundum and perovskite [8], with the goal of gaining insights into the O isotopic composition of the nebular gas(es) from which these CAIs condensed. As MIL 090019 is a classified as CO3.1, it shows some signs of thermal metamorphism, compared to the more primitive CO3 meteorites (e.g., DOM 08004/06). A second goal of this study is to search for evidence of nebular processes in phases such as perovskite and melilite that are susceptible to parent body alteration to varying degrees.

We analyzed the oxygen isotopic compositions of various CAIs from the MIL 090019 CO3 carbonaceous chondrite by ion imaging using the NanoSIMS 50L (Nano Secondary Ion Mass Spectrometer) at JSC following methods described in [9]. An advantage of ion imaging over traditional spot analyses is that it provides spatial context to the oxygen isotopic data. This work builds on previously reported oxygen isotopic composition of two other CAIs (CAI-44 and CAI-E2) from the same meteorite thin section [10, 11] (see Ross et al., this meeting).

Sample Description: The mineralogical and petrological characterization of CAIs from MIL 090019 chondrite was performed using the JOEL Hyperprobe 8530 electron microprobe at NASA JSC. Three refractory inclusions of varying mineralogy were targeted for isotopic study. CAI-2 is an ultra-refractory inclusion that contains corundum, perovskite, melilite, anorthite, and spinel. CAI-3 is an elongated inclusion that has spinel plus minor melilite, perovskite in the core and a rim containing melilite, Ti-Al-rich pyroxene, and diopside. CAI-E1 is a spherule containing hibonite, spinel, and perovskite in the core, and a melilite-rich mantle enveloped by a thin diopside rim.

Methods: Oxygen isotopic imaging of the CAIs was performed using the Cameca NanoSIMS 50L ion microprobe at NASA JSC. The O-isotopic maps were acquired by rastering a ~1.5-3 pA primary Cs^+ beam at 16 keV over an area of 20 × 20 μm for 80 image planes (over a period of ~5-7 hours). Negative secondary ions of $^{16}O^-$, $^{17}O^-$, $^{18}O^-$, $^{28}Si^-$, $^{24}Mg^{16}O^-$, $^{27}Al^{16}O^-$, and $^{40}Ca^{16}O^-$ were simultaneously acquired using electron multiplier detectors at a mass resolving power of >10,000, sufficient to resolve the $^{16}OH^-$ interference from the $^{17}O^-$ peak. An electron flood gun was used to mitigate sample charging during the analyses. We used San Carlos olivine and Madagascar hibonite as isotopic standards to correct for the instrumental mass fractionation. The O-isotopic ratios were corrected for the quasi simultaneous arrival (QSA) effect and the detector dead time. All reported errors are 1 sigma.

Results: In CAI-2 (Fig. 1), corundum shows ^{16}O-rich composition with $\Delta^{17}O$ values ranging from -23.0 to -14.8‰ whereas melilite shows intermediate O-isotopic composition ($\Delta^{17}O$ = -10.2 ± 7.1‰). The perovskite grains also show intermediate O-isotopic compositions with $\Delta^{17}O$ values ranging from -14 to -9‰. The matrix around this CAI has $\Delta^{17}O$ = -4.5 ± 2.7‰.

In CAI-3 (Fig. 2), perovskite, melilite, Ti-Al-rich pyroxene, diopside, and spinel have O-isotopic compositions ($\Delta^{17}O$ values) = -26.9 ± 4.5‰, -19.3 ± 3.4‰, -20.0 ± 4.3‰, -24.4 ± 4.9‰, and -22.4 ± 4.3 ‰, respectively.

In CAI-E1 (Fig. 3), both spinel and hibonite show ^{16}O-rich composition with $\Delta^{17}O$ values = -22.4 ± 2.9‰ and -20.9 ± 3.3‰, respectively whereas melilite shows intermediate O-isotopic composition ($\Delta^{17}O$ = -19.6 ± 2.6‰). The two perovskite grains analyzed in this inclusion show intermediate ^{16}O compositions ($\Delta^{17}O$ = -7.2 ± 3.4‰ and -13.8 ± 3.6‰). The matrix surrounding this inclusion exhibits a $\Delta^{17}O$ = -4.1 ± 4.4‰.

Discussion: The CAIs analyzed here and by us previously for the O-isotopic composition vary significantly in their mineralogy, including an ultra-refractory corundum-bearing CAI (CAI-2), hibonite and grossite-rich CAIs (CAI-E1 and previously reported CAI-44 [10]), and a spinel-melilite-rich inclusion (CAI-3). However, the same mineral phases display consistent

O-isotopic compositions across the various CAIs, i.e., spinel, hibonite, and pyroxene show ^{16}O-rich compositions whereas melilite shows a consistent intermediate O-isotopic composition. However, the O-isotopic composition of perovskite ranges from ^{16}O-rich (CAI-44 and CAI-3 ~ -25‰), to relatively ^{16}O-poor (CAI-2 and CAI-E1 ~ -10‰). This variation could be explained by three possible scenarios: (1) The perovskites sampled in these CAIs represent distinct reservoirs in the nebula, (2) All the perovskites condensed from ^{16}O-rich nebular gas and equilibrated with the ^{16}O-poor nebular gas to varying degree, and (3) All the perovskites condensed from ^{16}O-rich nebular gas and exchanged oxygen with ^{16}O-poor fluids on the meteorite parent body.

Among all the CAI minerals analyzed in this study, perovskite exhibits the fastest oxygen diffusion [12], followed by melilite [3], whereas mineral phases such as spinel and pyroxene are most resistant to oxygen diffusion [13]. Perovskite grains from all the CAIs show variable O-isotopic composition irrespective of their host phases. Specifically, ^{16}O-rich perovskites in CAI-3 and CAI-44 are surrounded by melilite, spinel, and hibonite. As the O-isotopic composition of the included perovskite grains do not correlate with the oxygen diffusion coefficients of the host minerals, late-stage O-isotopic equilibration in the nebula (after CAI-formation) or on the meteorite parent body is unlikely. Therefore, the variation seen in these perovskites are either primordial and reflect condensation from distinct early Solar System reservoirs or early ^{16}O-rich perovskites partially equilibrated with a ^{16}O-poor nebular gas to varying degree prior to incorporation by their host CAIs.

References: [1] Amelin Y. et al. (2010) *EPSL*, 300:343-350, [2] Connelly J. N. et al. (2012) *Science*, 338:651-655. [3] Yurimoto H. et al. (1998) *Science*, 282:1874-1877. [4] Krot, A. N., et al. (2004) GCA, 68(9):2167-2184. [5] Simon, S. B., & Grossman, L. (2015) *MAPS*, 50(6):1032-1049. [6] Simon, S. B., & Grossman, L. (2015) *MAPS* 50(6):1032-1049. [7] Han, J. (2014) (PhD thesis). [8] Grossman, L. (1972) GCA, 36(5):597-619. [9] Ito M. & Messenger S. (2008) *Appl. Surf. Sci.* 255:1446-1450. [10] Mane P. et al. (2019) the *82nd Annual Meeting of The Meteoritical Society* Abstr #2157. [11] Simon, J. I. et al. (2019). *The Astrophysical Journal Letters*, 884(2): L29. [12] Gautason, B., & Muehlenbachs, K. (1993) *Science*, 260(5107):518-521. [13] Ryerson, F. J., & McKeegan, K. D. (1994) *GCA* 58(17):3713-3734.

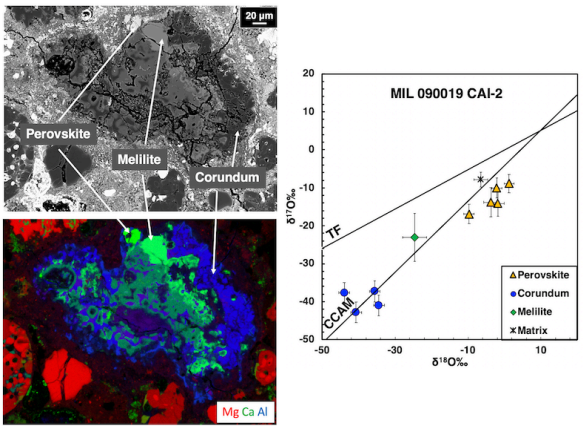

Figure 1. The backscatter electron image, X-ray elemental map highlighting different minerals phases, and the oxygen isotopic composition of different mineral phases in CAI-2 (with 1σ errors).

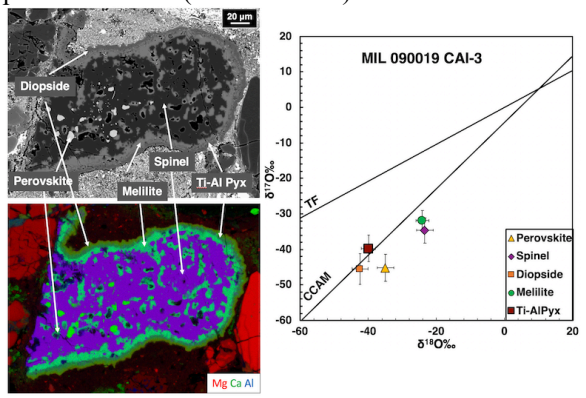

Figure 2. The backscatter electron image, X-ray elemental map highlighting different minerals phases, and the oxygen isotopic composition of different mineral phases in CAI-3 (with 1σ errors).

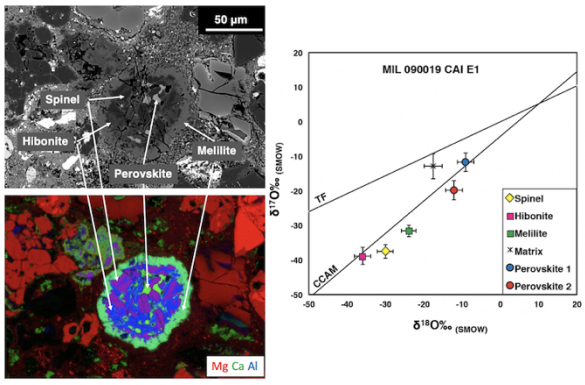

Figure 3. The backscatter electron image, X-ray elemental map highlighting different minerals phases, and the oxygen isotopic composition of different mineral phases in CAI-E1 (with 1σ errors).